

A Closed-Loop Linear Covariance Framework for Vehicle Path Planning in an Uncertain Obstacle Field

Randall S Christensen ^{*} and Greg Droke[†]
Utah State University, Logan, Utah, 84322, USA

Robert C. Leishman[‡]
Air Force Institute of Technology, Wright-Patterson AFB, OH, 45433, USA

Path planning in uncertain environments is a key enabler of true vehicle autonomy. Over the past two decades, numerous approaches have been developed to account for errors in the vehicle path while navigating complex and often uncertain environments. An important capability of such planning is the prediction of vehicle dispersion covariances about candidate paths. This work develops a new closed-loop linear covariance (CL-LinCov) framework applicable to wide range of autonomous system architectures. Extensions to current CL-LinCov frameworks are made to accommodate 1) the cascaded architecture typical of autonomous vehicles and 2) the dual-use of continuous sensor information for both navigation and control. The closed-loop nature of the framework preserves the important coupling between the system dynamics, exogenous disturbances, and the guidance, navigation, and control algorithms. The developed framework is applied to a simplified model of an unmanned aerial vehicle and validated by comparison via Monte Carlo analysis. The utility of the CL-LinCov information is illustrated by its application to path planning in an uncertain obstacle field via a modified version of the rapidly exploring random tree algorithm.

I. Introduction

AUTONOMOUS vehicles are quickly becoming integral parts of both civilian and military systems. An important component of such systems is the ability to safely plan the path of the vehicle to achieve mission objectives. Robust path planning must account for the dispersion of the vehicle about the planned path as well as the uncertainty in obstacles and/or adversarial systems. An important aspect of the dispersions is the coupled nature of the vehicle dynamics and the guidance, navigation, and control (GNC) systems. Neglecting this coupling often leads to risk probabilities that are overly optimistic or altogether incorrect [1]. Monte Carlo analysis is the status-quo method for assessing uncertainty in complex GNC systems. Given a large number of simulations (500+), the computed statistics

^{*}Assistant Professor, Department of Electrical and Computer Engineering, Randall.Christensen@usu.edu

[†]Assistant Professor, Department of Electrical and Computer Engineering, Greg.Droke@usu.edu

[‡]Director, Autonomy and Navigation Technology Center, Robert.Leishman@afit.edu

are accurate and a good representation of overall system performance. In the case of vehicle path planning, however, the number of candidate paths considered is often very large, precluding the use of Monte Carlo analysis for mission planning in general, and especially for real-time mission planning or situations with large numbers of cooperating vehicles. Thus, there is a need for a framework that produces dispersions statistics in a manner that is efficient for these more demanding scenarios.

Closed-loop Linear Covariance (CL-LinCov) analysis provides an efficient means for predicting the covariance of vehicle dispersions along a nominal trajectory. Under assumptions of Gaussian error sources and locally-linear dynamics and GNC algorithms, CL-LinCov produces the same statistical information as Monte Carlo analysis, but does so in a single run [2]. This work exploits the efficiency of CL-LinCov to plan the path of an autonomous vehicle through an uncertain obstacle field. A new CL-LinCov framework is developed, applicable to a wide range of autonomous vehicles, then validated for the specific case of a Dubins vehicle with drag, gust, and torque disturbances. Once validated, the dispersion covariance from the CL-LinCov framework is combined with obstacle location uncertainty to compute the probability of collision along candidate paths of a Rapidly-exploring Random Tree (RRT).

The remainder of this paper is organized as follows. A review of relevant literature is provided in Section II. Section III defines the Monte Carlo and LinCov frameworks with sufficient complexity to model a wide variety of autonomous vehicles. Section IV defines the dynamics, GNC models for the vehicle considered in this research. Section V discusses the modeling of uncertain obstacles and the augmentation of the RRT algorithm. Section VI presents simulation results which validate the LinCov framework and demonstrate its use for vehicle path planning. Conclusions are summarized in Section VII with lengthy derivations included in the appendix.

II. Literature Review

This section presents an overview of related literature, to provide context and motivation for the improvements made to CL-LinCov architectures and the associated application to path planning in uncertain environments.

A. Random Sampling

Recent years have seen an explosive growth in sample-based motion planning techniques for dealing with complex, partially known environments and systems with complicated dynamics. Near the turn of the century, the idea of a Rapidly-exploring Random Tree (RRT) was introduced as a means to quickly find a feasible path from a given starting point to a particular destination. As its name suggests, the RRT allows for a rapid search through high-dimensional spaces. In its most simple form, this algorithm iteratively builds a tree while randomly searching through the environment. In each iteration, a point is randomly selected and the nearest point on the tree is used to attempt to connect to the newly selected point. When an obstacle precludes the actual connecting of the tree to the new point, a point along the new path prior to the obstacle intersection is added to the tree. The RRT exhibits useful properties, two of which are probabilistic

completeness and an exponentially-decaying probability of failure [3].

One of the aspects that makes RRT such a versatile planner is that it is expressed in terms of a number of primitive procedures. Karaman and Frazzoli present a concise overview of many of these procedures for describing RRT. *Sample* selects a new point, *Nearest* finds vertices in the tree close to a particular point, and *Steer* attempts to connect different points. Many of the advancements in RRT, and its optimal counterpart RRT*, have focused on improvements to these primitives [4–9]. Common to all RRT planners is the *CollisionFree* primitive, which verifies the absence of obstacles along a candidate path. In this research, a new CL-LinCov framework is utilized to accommodate uncertainty in the *CollisionFree* primitive.

B. Planning Under Uncertainty

The concept of accounting for uncertainty in path planning is not new. It is often referred to as “chance-constrained” motion planning [10], in which traditional planners are extended to account for stochastic deviations of the vehicle from the candidate trajectory. In [11], the authors utilize an augmented state system, consisting of truth state dispersion and navigation errors, to predict the future covariance and calculate the “quality” of the candidate path. Similarly, [12] utilizes a linear covariance framework of truth and navigation states, paired with a genetic algorithm optimizer, to design robust trajectories for satellite rendezvous. In contrast, the authors of [1] modify the *estimation error* covariance matrix, obtained from the Extended Kalman Filter (EKF), to determine the distribution of state dispersions for all possible future state estimates. In [13], the collision chance constraints are transformed into deterministic constraints and incorporated into a model-predictive control law. Finally, the authors of [14] utilize concepts of probabilistic zonotopes and stochastic reachability to handle both bounded and stochastic measurement errors.

Although the cited methods differ in their approach, an important concept common to all is a method for predicting vehicle dispersions along candidate paths. This quantity is critical in determining the “chance constraint”, be it a collision with obstacles, collisions between vehicles, or a requirement on the final state dispersions. An important consideration when predicting vehicle dispersions is to account for the coupled relationship between state estimation errors and truth state dispersions. This coupling is determined by the guidance and control laws, and is especially important for the closed-loop systems. The focus of this research, therefore, is to extend the generality of CL-LinCov frameworks, to handle a broader range of GNC system architectures.

C. Efficient Statistical Framework for Closed-Loop GNC Systems

As mentioned previously, a critical metric for path planning in uncertainty, is the predicted dispersion of the vehicle about a candidate path. For nonlinear systems with large uncertainties, sample-based Monte Carlo approaches are the status quo for generating such metrics. The variance is estimated from ensembles obtained through numerous executions of a simulation, with varying initial conditions and noise sources. Since the statistics are estimated from samples of the

population, a large number is required for reasonable confidence intervals [15].

Linear covariance (LinCov) analysis has commonly been used to overcome the high computational requirements of Monte Carlo analysis. Historically, applications of LinCov have focused on open-loop vehicle dispersions due to exogenous disturbances or estimation errors for inertial navigation systems. More recent developments account for the coupled nature of the system dynamics with the GNC algorithms [15–19]. To differentiate from ‘open-loop’ frameworks, the approach used in this research is denoted as closed-loop LinCov (CL-LinCov). More details regarding the historical background of CL-LinCov and a tutorial are provided in [15]. Rather than compute the dispersion statistics from samples, CL-LinCov directly propagates the covariance of an augmented system, which contains both the vehicle dispersions and navigation errors, along a nominal trajectory. As such, CL-LinCov is well-suited to vehicle path planning, especially in scenarios where the time response of the guidance and control algorithms is significant, when compared to the obstacle field [1].

D. Contributions

The primary contribution of this paper is the extension, and subsequent validation, of CL-LinCov architectures to support path planning of autonomous vehicles in an uncertain obstacle field. A new CL-LinCov framework is developed which separates the high-level guidance algorithms from the low-level control. This architecture is typical of cascaded autopilots employed in UAV’s [7]. Furthermore, the developed framework accommodates continuous sensors used for both navigation state propagation as well as controller feedback. This is also typical of UAV autopilots, where rate gyros are used in the EKF to propagate attitude states, as well as in the low-level controllers to damp angular rates. The secondary contribution of this paper is an application of the CL-LinCov framework in the RRT path planner for an uncertain obstacle field. A linear transformation of the CL-LinCov framework is used to compute the dispersion covariance, relative to uncertain obstacles, along a candidate trajectory. The *CollisionFree* primitive utilizes this relative covariance to identify paths which maintain the probability of collision below user-selected bounds.

III. General Framework

This section develops the general framework for a closed-loop GNC system of sufficient complexity to model the vehicle outlined in Section IV. The developed framework is similar to one developed previously [15], with two notable extensions. First, a nonlinear guidance law is included which provides the set-point for the low-level control algorithms. Second, the low-level control algorithms are an explicit function of the same continuous measurements used for propagation of the navigation states. In contrast to the previous work [15], this enables control laws typical of UAVs, where the gyros are used both in the rate damping loop of the controller, as well as in propagation of attitude estimates [7]. Dual-use of the continuous measurements requires additional derivation steps not performed in previous publications [2, 15–17, 20].

A. Nonlinear Models

The general form of the nonlinear equations that define the dynamics and GNC system are developed here. The truth dynamics evolve based on the truth states of the system, $\mathbf{x} \in \mathbb{R}^n$, the input $\mathbf{u} \in \mathbb{R}^{n_u}$, and white noise $\mathbf{w} \in \mathbb{R}^{n_w}$ with power spectral density (PSD) S_w according to

$$\dot{\mathbf{x}} = \mathbf{f}(\mathbf{x}, \mathbf{u}, \mathbf{w}) \quad (1)$$

Observations of the truth state of the system are made through measurements, both in continuous time and discrete time. Continuous measurements $\tilde{\mathbf{y}} \in \mathbb{R}^{n_y}$, are corrupted by continuous white noise $\boldsymbol{\eta}$ with PSD S_η . Similarly, discrete measurements, $\tilde{\mathbf{z}} \in \mathbb{R}^{n_z}$, are corrupted by discrete noise $\boldsymbol{\nu}_k$ with variance R_ν .

$$\tilde{\mathbf{y}} = \mathbf{c}(\mathbf{x}, \mathbf{u}) + \boldsymbol{\eta} \quad (2)$$

$$\tilde{\mathbf{z}}_k = \mathbf{h}(\mathbf{x}_k) + \boldsymbol{\nu}_k \quad (3)$$

The navigation state, $\hat{\mathbf{x}} \in \mathbb{R}^{\hat{n}}$ is propagated using the continuous inertial measurements (commonly referred to as “model replacement” [21]), and updated via the Kalman gain \hat{K}_k and the residual $\tilde{\mathbf{z}}_k - \hat{\mathbf{z}}_k$, the difference between the discrete measurement and the predicted discrete measurement $\hat{\mathbf{z}} \in \mathbb{R}^{n_z}$

$$\dot{\hat{\mathbf{x}}} = \hat{\mathbf{f}}(\hat{\mathbf{x}}, \tilde{\mathbf{y}}) \quad (4)$$

$$\hat{\mathbf{x}}_k^+ = \hat{\mathbf{x}}_k^- + \hat{K}_k [\tilde{\mathbf{z}}_k - \hat{\mathbf{z}}_k] \quad (5)$$

$$\hat{\mathbf{z}}_k = \hat{\mathbf{h}}(\hat{\mathbf{x}}_k) \quad (6)$$

$$\hat{K}_k = \hat{P}_k^- \hat{H}_k \left(\hat{H}_k \hat{P}_k^- \hat{H}_k^T + \hat{R}_\nu \right)^{-1} \quad (7)$$

The navigation state covariance \hat{P} is propagated via the continuous Riccati equation and updated using the Joseph form

$$\dot{\hat{P}} = \hat{F} \hat{P} + \hat{P} \hat{F}^T + \hat{B} \hat{Q} \hat{B}^T \quad (8)$$

$$\hat{P}_k^+ = (I - \hat{K}_k \hat{H}_k) \hat{P}_k^- (I - \hat{K}_k \hat{H}_k)^T + \hat{K}_k \hat{R}_\nu \hat{K}_k^T \quad (9)$$

The quantities $\hat{\mathbf{f}}$, $\hat{\mathbf{h}}$, \hat{F} , \hat{H} , \hat{Q} , and \hat{R}_ν are all obtained from the navigation design model and are allowed to differ from the true values.

In many problems, the truth state vector is a more comprehensive description of the system and is therefore larger and possibly of a different form than the navigation state vector. The function \mathbf{m} provides the mapping between these

states and is useful in determining the true navigation error covariance.

$$\mathbf{x}_n = \mathbf{m}(\mathbf{x}) \quad (10)$$

The guidance law is modeled as a potentially nonlinear function of the navigation state, and produces a desired navigation state $\hat{\mathbf{x}}^* \in \mathbb{R}^{\hat{n}^*}$.

$$\hat{\mathbf{x}}^* = \mathbf{n}(\hat{\mathbf{x}}) \quad (11)$$

It is important to note that the guidance algorithm does not, in general, specify the desired value for all components of the state vector. It is therefore of size \hat{n}^* which is not necessarily equal to \hat{n} . To enable modeling of output feedback control laws (e.g. PID controllers), a control state $\check{\mathbf{x}} \in \mathbb{R}^{\hat{n}}$ is defined with a dynamics equation $\check{\mathbf{f}}$ and an output equation \mathbf{g} . $\mathbf{u} \in \mathbb{R}^{n_u}$

$$\dot{\check{\mathbf{x}}} = \check{\mathbf{f}}(\check{\mathbf{x}}, \hat{\mathbf{x}}^*) \quad (12)$$

$$\mathbf{u} = \mathbf{g}(\check{\mathbf{x}}, \hat{\mathbf{x}}, \hat{\mathbf{x}}^*, \tilde{\mathbf{y}}) \quad (13)$$

It is important to note that the continuous measurement $\tilde{\mathbf{y}}$ in the Eq. (13) is the same quantity used to propagate the navigation state in Eq. (4)

B. Linear Modeling

To enable direct covariance calculations, this section linearizes the system in Section III.A about a nominal reference trajectory. An important concept in the linearization is the dispersion of the truth, navigation, and controller states. The dispersions are defined as the difference between the state and its corresponding nominal, denoted by an over-bar.

$$\delta \mathbf{x} = \mathbf{x} - \bar{\mathbf{x}} \quad (14)$$

$$\delta \hat{\mathbf{x}} = \hat{\mathbf{x}} - \bar{\hat{\mathbf{x}}} \quad (15)$$

$$\delta \check{\mathbf{x}} = \check{\mathbf{x}} - \bar{\check{\mathbf{x}}} \quad (16)$$

There are multiple ways, in practice, to compute the nominal. For this research, the nominal is computed as the trajectory of the states when all noise sources are deactivated in the simulation. The remainder of this section linearizes the system defined in Section III.A about the nominal trajectory. For this effort, it is desired to obtain a coupled, linear state space system in the dispersion variables, $\delta \mathbf{x}$, $\delta \hat{\mathbf{x}}$, and $\delta \check{\mathbf{x}}$. This can be obtained via partial derivatives or perturbation techniques. For this development, it is assumed that partial derivatives exist and can be utilized in the linearization. Regarding notation, F_x , denotes the partial derivative of the vector function f with respect to the vector \mathbf{x} ,

evaluated along the nominal trajectory,

$$F_x = \left. \frac{\partial f}{\partial x} \right|_{x=\bar{x}, \hat{x}=\hat{\bar{x}}, \check{x}=\check{\bar{x}}} \quad (17)$$

In the event that partial derivatives are difficult or impossible to derive, terms such as F_x refer to the coefficient matrix obtained via alternative linearization techniques.

The differential equations describing the dynamics of the truth state Eq. (1), navigation state Eq. (4), and controller state Eq. (11) are linearized to produce the corresponding perturbation differential equations.

$$\begin{aligned} \delta \dot{x} &= (F_x + F_u S G_{\bar{y}} C_x) \delta x \\ &+ (F_u S G_{\hat{x}} + F_u S G_{\hat{x}^*} N_{\hat{x}}) \delta \hat{x} \\ &+ F_u S G_{\check{x}} \delta \check{x} + F_u S G_{\bar{y}} \eta + B w \end{aligned} \quad (18)$$

$$\begin{aligned} \delta \dot{\hat{x}} &= \hat{F}_{\bar{y}} T C_x \delta x \\ &+ (\hat{F}_{\hat{x}} + \hat{F}_{\bar{y}} T C_u G_{\hat{x}} + \hat{F}_{\bar{y}} T C_u G_{\hat{x}^*} N_{\hat{x}}) \delta \hat{x} \\ &+ \hat{F}_{\bar{y}} T C_u G_{\check{x}} \delta \check{x} + \hat{F}_{\bar{y}} T \eta \end{aligned} \quad (19)$$

$$\delta \dot{\check{x}} = (\check{F}_{\hat{x}} + \check{F}_{\hat{x}^*} N_{\hat{x}}) \delta \hat{x} \quad (20)$$

where,

$$S = (I_{n_u \times n_u} - G_{\bar{y}} C_u)^{-1} \quad (21)$$

$$T = (I_{n_y \times n_y} - C_u G_{\bar{y}})^{-1} \quad (22)$$

The navigation state update (5) is also linearized along with (6) to produce the following set of dispersion update equations

$$\delta x_k^+ = \delta x_k^- \quad (23)$$

$$\delta \hat{x}_k^+ = (I_{\hat{n} \times \hat{n}} - \hat{K}_k \hat{H}_{\hat{x}}) \delta \hat{x}_k^- + \hat{K}_k H_x \delta x_k^- + \hat{K}_k \nu_k \quad (24)$$

$$\delta \check{x}_k^+ = \delta \check{x}_k^- \quad (25)$$

where it is noted that the truth and controller state dispersions are not directly affected by the update of the navigation state. The derivation of the preceding dispersion propagation and update equations are documented in detail in Section VII.A.

Once linearized, the augmented state vector is formed as

$$X = \begin{bmatrix} \delta x \\ \delta \hat{x} \\ \delta \check{x} \end{bmatrix} \quad (26)$$

With this definition, the augmented propagation and update equations become

$$\dot{X} = \mathcal{F}X + \mathcal{G}\eta + \mathcal{W}w \quad (27)$$

$$X_k^+ = \mathcal{A}_k X_k^- + \mathcal{B}_k v_k \quad (28)$$

where

$$\mathcal{F} = \begin{bmatrix} \mathcal{F}_{xx} & \mathcal{F}_{x\hat{x}} & \mathcal{F}_{x\check{x}} \\ \mathcal{F}_{\hat{x}x} & \mathcal{F}_{\hat{x}\hat{x}} & \mathcal{F}_{\hat{x}\check{x}} \\ 0_{\check{x} \times n} & \mathcal{F}_{\check{x}\hat{x}} & 0_{\check{x} \times \check{x}} \end{bmatrix} \quad (29)$$

$$\mathcal{G} = \begin{bmatrix} F_u S G_{\check{y}} \\ \hat{F}_{\check{y}} T \\ 0_{\check{y} \times n_{\check{y}}} \end{bmatrix} \quad (30)$$

$$\mathcal{W} = \begin{bmatrix} B \\ 0_{\hat{n} \times n_w} \\ 0_{\check{n} \times n_w} \end{bmatrix} \quad (31)$$

$$\mathcal{A}_k = \begin{bmatrix} I_{n \times n} & 0_{n \times \hat{n}} & 0_{n \times \check{n}} \\ \hat{K}_k H_x & I_{\hat{n} \times \hat{n}} - \hat{K}_k \hat{H}_{\hat{x}} & 0_{\hat{n} \times \check{n}} \\ 0_{\check{n} \times n} & 0_{\check{n} \times \hat{n}} & I_{\check{n} \times \check{n}} \end{bmatrix} \quad (32)$$

$$\mathcal{B}_k = \begin{bmatrix} 0_{n \times n_z} \\ \hat{K}_k \\ 0_{\check{n} \times n_z} \end{bmatrix} \quad (33)$$

And where the individual sub matrices of \mathcal{F} are defined as

$$\mathcal{F}_{xx} = F_x + F_u S G_{\tilde{y}} C_x \quad (34)$$

$$\mathcal{F}_{x\hat{x}} = F_u S G_{\hat{x}} + F_u S G_{\hat{x}^*} N_{\hat{x}} \quad (35)$$

$$\mathcal{F}_{x\check{x}} = F_u S G_{\check{x}} \quad (36)$$

$$\mathcal{F}_{\hat{x}x} = \hat{F}_{\tilde{y}} T C_x \quad (37)$$

$$\mathcal{F}_{\hat{x}\hat{x}} = \hat{F}_{\hat{x}} + \hat{F}_{\tilde{y}} T C_u G_{\hat{x}} + \hat{F}_{\tilde{y}} T C_u G_{\hat{x}^*} N_{\hat{x}} \quad (38)$$

$$\mathcal{F}_{\hat{x}\check{x}} = \hat{F}_{\tilde{y}} T C_u G_{\hat{x}} \quad (39)$$

$$\mathcal{F}_{\check{x}\hat{x}} = \check{F}_{\hat{x}} + \check{F}_{\hat{x}^*} N_{\hat{x}} \quad (40)$$

C. Performance Evaluation

With the augmented differential and update equations defined in Eqs. (27) and (28), the covariance propagation and update equations are expressed as

$$\dot{C}_A = \mathcal{F} C_A + C_A \mathcal{F}^T + \mathcal{G} S_\eta \mathcal{G}^T + \mathcal{W} S_w \mathcal{W}^T \quad (41)$$

$$C_A^+ = \mathcal{A}_k C_A^- \mathcal{A}_k^T + \mathcal{B}_k R_\nu \mathcal{B}_k^T \quad (42)$$

Two quantities of typical interest are the covariance of the truth state dispersions and the estimation errors. It is important to note that the estimation error covariance defined below is the true estimation error covariance, which may be different than the estimated quantity, \hat{P} , from the Kalman filter. These quantities are extracted from the augmented covariance matrix via the following equations.

$$D_{true} = \begin{bmatrix} I_{n \times n} & 0_{n \times \hat{n}} & 0_{n \times \check{n}} \end{bmatrix} C_A \begin{bmatrix} I_{n \times n} & 0_{n \times \hat{n}} & 0_{n \times \check{n}} \end{bmatrix}^T \quad (43)$$

$$P_{true} = \begin{bmatrix} -M_x & I_{\hat{n} \times \hat{n}} & 0_{\hat{n} \times \check{n}} \end{bmatrix} C_A \begin{bmatrix} -M_x & I_{\hat{n} \times \hat{n}} & 0_{\hat{n} \times \check{n}} \end{bmatrix}^T \quad (44)$$

IV. Vehicle Model

This section of the paper defines the nonlinear equations specific to the UAV system considered in this research. For demonstration purposes and mathematical tractability, this research utilizes the aircraft dynamics model found in [7],

reduced to the horizontal plane and with assumptions of constant altitude and zero side-slip. Despite the simplifications, the presented model has several key components of the more generic case of a full 6 degree-of-freedom model, and exercises all elements of the CL-LinCov framework developed in Section III. Where appropriate, the general equations from Section III are indicated below the corresponding equation for the UAV system.

A. Nonlinear Model

The truth state of the vehicle is defined by its north and east position (p_n, p_e), ground speed (V_g), heading (ψ), and angular rate (ω). The vehicle is disturbed by axial wind gust (u_w) and disturbance torques (T_d), which are also included in the truth state.

$$\mathbf{x} = \begin{bmatrix} p_n \\ p_e \\ V_g \\ \psi \\ \omega \\ u_w \\ T_{dist} \end{bmatrix} \quad (45)$$

The dynamics of the truth states incorporate the kinematic relationship between position and velocity, as well as heading and angular rate. Aerodynamic effects include drag and a Dryden gust model [22], which is assumed predominant in the axial direction. Finally the disturbance torques are modeled as a First-Order Gauss-Markov (FOGM) process.

$$\begin{bmatrix} \dot{p}_n \\ \dot{p}_e \\ \dot{V}_g \\ \dot{\psi} \\ \dot{\omega} \\ \dot{u}_w \\ \dot{T}_d \end{bmatrix} = \underbrace{\begin{bmatrix} V_g \cos \psi \\ V_g \sin \psi \\ \frac{1}{m} \left[F_c - \frac{1}{2} \rho C_{D0} S_p (V_g - u_w)^2 \right] \\ \omega \\ \frac{1}{J} (T_c + T_{dist}) \\ -\frac{V_g}{L_u} u_w + \sigma_u \sqrt{\frac{2V_g}{L_u}} w_u \\ -\frac{1}{\tau_T} T_d + w_T \end{bmatrix}}_{f(\mathbf{x}, \mathbf{u}, \mathbf{w})} \quad (46)$$

The control inputs to the vehicle are force (F_c) and torque (T_c)

$$\mathbf{u} = \begin{bmatrix} F_c \\ T_c \end{bmatrix} \quad (47)$$

Finally, the white process noise includes the driving noise for the Dryen gust model and the disturbance torque FOGM process

$$\mathbf{w} = \begin{bmatrix} w_u \\ w_T \end{bmatrix} \quad (48)$$

The continuous measurements corresponding to Eq. (2), which are used to propagate the navigation state, consist of an accelerometer aligned with the direction of travel, and a gyro aligned with the local vertical, corrupted by continuous white noise.

$$\underbrace{\begin{bmatrix} \tilde{a}_x \\ \tilde{\omega} \end{bmatrix}}_{\tilde{\mathbf{y}}} = \underbrace{\begin{bmatrix} a + \eta_a \\ \omega + \eta_\omega \end{bmatrix}}_{\mathbf{c}(\mathbf{x}, \mathbf{u})} \quad (49)$$

where the true acceleration of the vehicle is a function of the control input (\mathbf{u})

$$a = \frac{1}{m} \left\{ F_{control} - \frac{1}{2} \rho C_{D_0} S_p (V_g - u_w)^2 \right\} \quad (50)$$

Corresponding to Eq. (3), the discrete measurements available to the inertial navigation system are comprised of horizontal position and ground speed, corrupted by discrete white noise.

$$\underbrace{\begin{bmatrix} \tilde{p}_n [t_k] \\ \tilde{p}_e [t_k] \\ \tilde{V}_g [t_k] \end{bmatrix}}_{\tilde{\mathbf{z}}_k} = \underbrace{\begin{bmatrix} p_n [t_k] \\ p_e [t_k] \\ V_g [t_k] \end{bmatrix}}_{\mathbf{h}(\mathbf{x}_k)} + \underbrace{\begin{bmatrix} v_n [t_k] \\ v_e [t_k] \\ v_V [t_k] \end{bmatrix}}_{\mathbf{v}_k} \quad (51)$$

The navigation state vector is a subset of the truth states, including only position, ground speed, and heading states.

$$\hat{\mathbf{x}} = \begin{bmatrix} \hat{p}_n \\ \hat{p}_e \\ \hat{V}_g \\ \hat{\psi} \end{bmatrix} \quad (52)$$

Since the vehicle has no knowledge of control and disturbance inputs, the navigation states are propagated using the so-called “model replacement” technique [21], where sensed accelerations and angular rates are utilized in lieu of the unknown inputs, corresponding to Eq. (4).

$$\underbrace{\begin{bmatrix} \dot{\hat{p}}_n \\ \dot{\hat{p}}_e \\ \dot{\hat{V}}_g \\ \dot{\hat{\psi}} \end{bmatrix}}_{\dot{\hat{\mathbf{x}}}} = \underbrace{\begin{bmatrix} \hat{V}_g \cos \hat{\psi} \\ \hat{V}_g \sin \hat{\psi} \\ a + \eta_a \\ \omega + \eta_\omega \end{bmatrix}}_{\hat{f}(\hat{\mathbf{x}}, \hat{\mathbf{y}})} \quad (53)$$

Finally, the predicted discrete measurements, corresponding to Eq. (6) is equivalent to Eq. (51), but omitting the unknown measurement noise.

$$\underbrace{\begin{bmatrix} \hat{p}_n [t_k] \\ \hat{p}_e [t_k] \\ \hat{V}_g [t_k] \end{bmatrix}}_{\hat{\mathbf{z}}} = \underbrace{\begin{bmatrix} \hat{p}_n [t_k] \\ \hat{p}_e [t_k] \\ \hat{V}_g [t_k] \end{bmatrix}}_{\hat{\mathbf{h}}(\hat{\mathbf{x}})} \quad (54)$$

The matrices utilized in Eqs. (7) to (9) are derived by linearization of the preceding navigation models

$$\hat{F} = \begin{bmatrix} 0 & 0 & \cos \hat{\psi} & -\hat{V}_g \sin \hat{\psi} \\ 0 & 0 & \sin \hat{\psi} & \hat{V}_g \cos \hat{\psi} \\ 0 & 0 & 0 & 0 \\ 0 & 0 & 0 & 0 \end{bmatrix} \quad (55)$$

$$\hat{H}_k = \begin{bmatrix} 1 & 0 & 0 & 0 \\ 0 & 1 & 0 & 0 \\ 0 & 0 & 1 & 0 \end{bmatrix} \quad (56)$$

$$\hat{R}_v = \begin{bmatrix} \hat{\sigma}_n^2 & 0 & 0 \\ 0 & \hat{\sigma}_e^2 & 0 \\ 0 & 0 & \hat{\sigma}_v^2 \end{bmatrix} \delta_{ij} \quad (57)$$

$$\hat{B} = \begin{bmatrix} 0 & 0 \\ 0 & 0 \\ 1 & 0 \\ 0 & 1 \end{bmatrix} \quad (58)$$

$$\hat{Q} = \begin{bmatrix} \hat{Q}_a & 0 \\ 0 & \hat{Q}_\omega \end{bmatrix} \delta(t - t') \quad (59)$$

It remains to define the guidance and low-level control laws of the UAV path following system. The guidance law is based on the straight-line path guidance presented in [7]. The output of the guidance laws comprises a constant commanded ground speed (V_g^*) and a vehicle heading (ψ^*) which directs the UAV to the straight line

$$\hat{x}^* = \begin{bmatrix} V_g^* \\ \psi^* \end{bmatrix} = \underbrace{\begin{bmatrix} \bar{V}_g \\ \psi_q - \psi^\infty \frac{2}{\pi} \arctan(k_{path} e_{path}) \end{bmatrix}}_{n(\hat{x})} \quad (60)$$

where ψ_q is the path heading and e_{path} is the deviation of the vehicle from the desired path, in the cross-track direction

$$e_{path} = (-\sin \psi_q (\hat{p}_n - r_n) + \cos \psi_q (\hat{p}_e - r_e)) \quad (61)$$

The parameters ψ^∞ and k_{path} determine the response of the guidance law to cross-track errors. The path unit vector q^{ned} and origin $\mathbf{r} = \begin{bmatrix} r_n & r_e \end{bmatrix}^T$ are determined by

$$\mathbf{r} = \mathbf{w}_{i-1} \quad (62)$$

$$\mathbf{q}^{ned} = \frac{\mathbf{w}_{i+1} - \mathbf{w}_i}{\|\mathbf{w}_{i+1} - \mathbf{w}_i\|} \quad (63)$$

where \mathbf{w}_{i-1} , \mathbf{w}_i , and \mathbf{w}_{i+1} correspond to the previous, current, and subsequent way-points, respectively. The heading of the desired path ψ_q is calculated from the North and East components of the path unit vector

$$\psi_q = \text{atan2}(q_e, q_n) \quad (64)$$

The low-level control law corresponding to (12) and (13) is comprised of a state space system of integrator states

$$\underbrace{\begin{bmatrix} \dot{\sigma}_F \\ \dot{\sigma}_T \end{bmatrix}}_{\dot{\mathbf{x}}} = \underbrace{\begin{bmatrix} V_g^* - \hat{V}_g \\ \psi^* - \hat{\psi} \end{bmatrix}}_{\check{f}(\hat{\mathbf{x}}, \hat{\mathbf{x}}^*)} \quad (65)$$

and an output equation

$$\mathbf{u} = \begin{bmatrix} F_c \\ T_c \end{bmatrix} = \underbrace{\begin{bmatrix} P_F (V_g^* - \hat{V}_g) + I_F \sigma_F \\ D_T \{P_T (\psi^* - \hat{\psi}) + I_T \sigma_T - \tilde{\omega}\} \end{bmatrix}}_{g(\hat{\mathbf{x}}, \hat{\mathbf{x}}^*, \tilde{\mathbf{y}})} \quad (66)$$

where P_F and I_F are the proportional and integral control gains of the velocity controller. Similarly, P_T , I_T , and D_T are the proportional, integral, and derivative gains of the heading controller. Finally the mapping between truth states and navigation states corresponding to Eq. (10) is simply

$$\begin{bmatrix} p_n \\ p_e \\ V_g \\ \psi \end{bmatrix} = \begin{bmatrix} I_{4 \times 4} & 0_{4 \times 3} \end{bmatrix} \begin{bmatrix} p_n \\ p_e \\ V_g \\ \psi \\ \omega \\ F_{dist} \\ T_{dist} \end{bmatrix} = \mathbf{m}(\mathbf{x}) \quad (67)$$

B. Linearized Model

The coefficient matrices in Eqs. (18) through (25) for the system under consideration are listed subsequently.

Linearization of (1) yields

$$F_x = \begin{bmatrix} 0 & 0 & \cos \bar{\psi} & -\bar{V}_g \sin \bar{\psi} & 0 & 0 & 0 \\ 0 & 0 & \sin \bar{\psi} & \bar{V}_g \cos \bar{\psi} & 0 & 0 & 0 \\ 0 & 0 & F_{V_g} & 0 & 0 & F_{u_w} & 0 \\ 0 & 0 & 0 & 0 & 1 & 0 & 0 \\ 0 & 0 & 0 & 0 & 0 & 0 & \frac{1}{J} \\ 0 & 0 & -\frac{\bar{u}_w}{L_u} & 0 & 0 & -\frac{\bar{V}_g}{L_u} & 0 \\ 0 & 0 & 0 & 0 & 0 & 0 & -\frac{1}{\tau_T} \end{bmatrix} \quad (68)$$

$$F_u = \begin{bmatrix} 0 & 0 \\ 0 & 0 \\ \frac{1}{m} & 0 \\ 0 & 0 \\ 0 & \frac{1}{J} \\ 0 & 0 \\ 0 & 0 \end{bmatrix} \quad (69)$$

$$B = \begin{bmatrix} 0 & 0 \\ 0 & 0 \\ 0 & 0 \\ 0 & 0 \\ 0 & 0 \\ \sigma_u \sqrt{\frac{2\bar{V}_g}{L_u}} & 0 \\ 0 & 1 \end{bmatrix} \quad (70)$$

where

$$F_{V_g} = -\frac{\rho C_{D_0} S_p (\bar{V}_g - \bar{u}_w)}{m} \quad (71)$$

$$F_{u_w} = \frac{\rho C_{D_0} S_p (\bar{V}_g - \bar{u}_w)}{m} \quad (72)$$

The partial derivatives of the controller output Eq. (13) are

$$G_{\bar{y}} = \begin{bmatrix} 0 & 0 \\ 0 & -D_T \end{bmatrix} \quad (73)$$

$$G_{\hat{x}} = \begin{bmatrix} 0 & 0 & -P_F & 0 \\ 0 & 0 & 0 & -D_T P_T \end{bmatrix} \quad (74)$$

$$G_{\hat{x}^*} = \begin{bmatrix} P_F & 0 \\ 0 & D_T P_T \end{bmatrix} \quad (75)$$

$$G_{\check{x}} = \begin{bmatrix} I_F & 0 \\ 0 & D_T I_T \end{bmatrix} \quad (76)$$

The partial derivatives of the continuous measurement function in Eq. (2) are

$$C_x = \begin{bmatrix} 0 & 0 & -\frac{\rho C_{D_0} S_p (\bar{V}_g - \bar{u}_w)}{m} & 0 & 0 & \frac{\rho C_{D_0} S_p (\bar{V}_g - \bar{u}_w)}{m} & 0 \\ 0 & 0 & 0 & 0 & 1 & 0 & 0 \end{bmatrix} \quad (77)$$

$$C_u = \begin{bmatrix} \frac{1}{m} & 0 \\ 0 & 0 \end{bmatrix} \quad (78)$$

The partial derivative of the guidance law of Eq. (11) is

$$N_{\hat{x}} = \begin{bmatrix} 0 & 0 & 0 & 0 \\ N_{21}/N_D & N_{22}/N_D & 0 & 0 \end{bmatrix} \quad (79)$$

where

$$N_{21} = 2\psi^\infty k_{path} \sin \psi_q \quad (80)$$

$$N_{22} = -2\psi^\infty k_{path} \cos \psi_q \quad (81)$$

$$N_D = \pi + \pi k_{path}^2 d^2 \quad (82)$$

$$d = -\sin \psi_q [\hat{p}_n - r_n] + \cos \psi_q [\hat{p}_e - r_e] \quad (83)$$

The partial derivatives of the navigation state propagation function in Eq. (4)

$$\hat{F}_{\hat{x}} = \begin{bmatrix} 0 & 0 & \cos \hat{\psi} & -\hat{V}_g \sin \hat{\psi} \\ 0 & 0 & \sin \hat{\psi} & \hat{V}_g \cos \hat{\psi} \\ 0 & 0 & 0 & 0 \\ 0 & 0 & 0 & 0 \end{bmatrix} \quad (84)$$

$$\hat{F}_{\hat{y}} = \begin{bmatrix} 0 & 0 \\ 0 & 0 \\ 1 & 0 \\ 0 & 1 \end{bmatrix} \quad (85)$$

The partials of the controller propagation function in Eq. (12) are

$$\check{F}_{\hat{x}} = \begin{bmatrix} 0 & 0 & -1 & 0 \\ 0 & 0 & 0 & -1 \end{bmatrix} \quad (86)$$

$$\check{F}_{\hat{x}^*} = \begin{bmatrix} 1 & 0 \\ 0 & 1 \end{bmatrix} \quad (87)$$

The partials of the truth and navigation measurement models in Eqs. (3) and (6) are

$$H_x = \begin{bmatrix} 1 & 0 & 0 & 0 & 0 & 0 & 0 \\ 0 & 1 & 0 & 0 & 0 & 0 & 0 \\ 0 & 0 & 1 & 0 & 0 & 0 & 0 \end{bmatrix} \quad (88)$$

$$\hat{H}_{\hat{x}} = \begin{bmatrix} 1 & 0 & 0 & 0 \\ 0 & 1 & 0 & 0 \\ 0 & 0 & 1 & 0 \end{bmatrix} \quad (89)$$

Finally, the partial of the mapping between truth and navigation states in Eq. (10) is simply

$$M_x = \begin{bmatrix} I_{4 \times 4} & 0_{4 \times 3} \\ 0_{3 \times 4} & 0_{3 \times 3} \end{bmatrix} \quad (90)$$

V. Path Planning

This section of the paper defines the approach for path planning in an uncertain obstacle field. A method is developed for computing the probability of collision from the truth state dispersion covariance and a probabilistic description of the obstacle field. This forms the basis of the *CollisionFree* primitive for the Rapidly-exploring Random Tree path planner.

A. Probability of Collision

The chance constraint considered in this research is the probability of collision between the vehicle and the uncertain obstacles. Many approaches exist for determining collision probabilities, depending on the shapes and relative sizes of the vehicle and obstacles [23–26]. When the vehicle is small compared to the obstacles, each obstacle can be modeled as a static object whose location follows a Gaussian distribution, and whose size is specified by a bounding box. The probability of collision for each individual obstacle is therefore computed as the probability that the vehicle is inside the bounding box [27]. To aid in understanding this paradigm of collision probability, two *scalar, independent* Gaussian random variables, representing the position of two objects, are considered

$$x \sim N(m_x, P_x) \quad (91)$$

$$y \sim N(m_y, P_y) \quad (92)$$

Combining the random variables as a vector yields

$$z = \begin{bmatrix} x & y \end{bmatrix}^T \in \mathbb{R}^2 \quad (93)$$

where the joint PDF is defined as

$$f_z(\zeta) = \frac{1}{N_z} \exp \left\{ -\frac{1}{2} [\zeta - \mathbf{m}_z]^T P_{zz}^{-1} [\zeta - \mathbf{m}_z] \right\} \quad (94)$$

$$N_z = 2\pi |P_{zz}|^{1/2} \quad (95)$$

Since the two random variables are independent, the mean and covariance of the joint distribution are simply the

augmentation of the individual parameters

$$\mathbf{m}_z = \begin{bmatrix} m_x & m_y \end{bmatrix}^T \quad (96)$$

$$P_{zz} = \begin{bmatrix} P_x & 0 \\ 0 & P_y \end{bmatrix} \quad (97)$$

The relative position of the two objects is computed as an linear operation on the random vector \mathbf{z}

$$d = A\mathbf{z} \quad (98)$$

where

$$A = \begin{bmatrix} 1 & -1 \end{bmatrix} \quad (99)$$

This corresponds to a new Gaussian random variable with the following mean, covariance, and probability density function [21]

$$m_d = A\mathbf{m}_z \quad (100)$$

$$P_d = AP_{zz}A^T \quad (101)$$

$$f_d(\delta) = \frac{1}{\sqrt{2\pi P_d}} \exp\left\{-\frac{1}{2P_d}(\delta - m_d)^2\right\} \quad (102)$$

Finally, the probability that the two objects are closer than a specified threshold l is simply the integration of f_d over $\delta = \pm l$

$$P(l) \equiv \int_{-l}^l f_d(\rho) d\rho \quad (103)$$

Extension of this collision probability paradigm to two dimensions with N obstacles is straightforward. The combined system is expressed as a random vector of the vehicle position p and the N obstacle positions

$$\mathbf{z} = \begin{bmatrix} \mathbf{p} \\ \mathbf{p}_1 \\ \mathbf{p}_2 \\ \vdots \\ \mathbf{p}_N \end{bmatrix} \in \mathbb{R}^{2(N+1)} \quad (104)$$

with probability density function, mean, and covariance defined by the following

$$f_z(\zeta) = \frac{1}{N_z} \exp \left\{ -\frac{1}{2} [\zeta - \mathbf{m}_z]^T P_{zz}^{-1} [\zeta - \mathbf{m}_z] \right\} \quad (105)$$

$$N_z = (2\pi)^{(N+1)} |P_{zz}|^{1/2} \quad (106)$$

$$\mathbf{m}_z = \begin{bmatrix} \mathbf{m}_{uav} \\ \mathbf{m}_1 \\ \mathbf{m}_2 \\ \vdots \\ \mathbf{m}_N \end{bmatrix} \quad (107)$$

$$P_{zz} = \text{diag} \left(\begin{bmatrix} P_{uav} & P_1 & P_2 & \cdots & P_N \end{bmatrix} \right) \quad (108)$$

The relative position of the vehicle with respect to obstacle, i , is again computed as a linear transformation of the random vector z

$$\mathbf{d} = A\mathbf{z} \quad (109)$$

where

$$A = \begin{bmatrix} & \\ I_{2 \times 2} & A_i \end{bmatrix} \quad (110)$$

$$A_i = \begin{bmatrix} & \\ 0_{2 \times 2(i-1)} & -I_{2 \times 2} & 0_{2 \times 2(N-i)} \end{bmatrix} \quad (111)$$

This corresponds to a new Gaussian random vector with the following mean, covariance, and distribution

$$\mathbf{m}_d = A\mathbf{m}_z \quad (112)$$

$$P_d = AP_{zz}A^T \quad (113)$$

$$f_d(\delta) = N_z \exp \left\{ -\frac{1}{2} [\delta - \mathbf{m}_d]^T P_{dd}^{-1} [\delta - \mathbf{m}_d] \right\} \quad (114)$$

$$N_z = \frac{1}{2\pi |P_{zz}|^{1/2}} \quad (115)$$

Finally, the probability that the vehicle is closer than the vector threshold \mathbf{l} is the integration of f_d over $\delta = \pm \mathbf{l}$

$$P(\mathbf{l}) \equiv \int_{-l_1}^{l_1} \int_{-l_2}^{l_2} f_d(l_1, l_2) dl_1 dl_2 \quad (116)$$

If a scalar distance is the more desirable metric, a new random variable can be defined as

$$\rho = \theta(\mathbf{d}) = (\mathbf{d}^T \mathbf{d})^{1/2} \quad (117)$$

However, since this new random variable is defined via a nonlinear transformation, the resulting distribution is no longer guaranteed to be Gaussian, and must be determined via the following

$$f_\rho(\xi) = f_{\mathbf{d}}[\theta^{-1}(\xi)] \|\partial\theta^{-1}(\xi)/\partial\xi\| \quad (118)$$

B. RRT with Probability of Collision Constraint

Many options exist for the path planning of a vehicle through an obstacle field. An excellent review of path planning in general, with a focus on sampling-based planners is provided in [28], where rapidly exploring random trees (RRT's) are cited as particularly suitable for vehicles with differential constraints, nonlinear dynamics, and non-holonomic constraints. The RRT algorithm implemented in this research is a combination of the RRT algorithms discussed in [7, 28], and is documented in Algorithm 1.

Algorithm 1: Rapidly Exploring Random Trees

Result: Shortest waypoint path \mathcal{W}

```

1 Initialize directed graph  $G = (V, E)$  where  $V = \left\{ \mathbf{x}_s, \mathbf{x}_f \right\}$ ,  $E = \emptyset$ 
2 Initialize obstacle map  $O = \{\mathbf{m}_i, P_i\}$ 
3 while  $i < N$  do
4    $\mathbf{x}_{rand} \leftarrow \text{Sample}(i)$ 
5    $\mathbf{x}_{nearest} \leftarrow \text{Nearest}(p, V)$ 
6    $\mathbf{x}_{new} \leftarrow \text{Steer}(\mathbf{x}_{nearest}, \mathbf{x}_{rand}, \lambda)$ 
7    $\mathbf{x}(t), \Delta t \leftarrow \text{RunSim}(\mathbf{x}_{nearest}, \mathbf{x}_{new})$ 
8   if  $\text{CollisionFree}(\mathbf{x}(t), O)$  then
9      $V \leftarrow V \cup \mathbf{x}_{new}$ 
10     $E \leftarrow E \cup \{(\mathbf{x}_{nearest}, \mathbf{x}_{new}), \Delta t\}$ 
11  end
12  if  $\|\mathbf{x}_{new} - \mathbf{x}_f\| \leq \lambda$  then
13     $\mathbf{x}(t), \Delta t \leftarrow \text{runsim}(\mathbf{x}_{new}, \mathbf{x}_f)$ 
14    if  $\text{CollisionFree}(\mathbf{x}(t), O)$  then
15       $V \leftarrow V \cup \mathbf{x}_f$ 
16       $E \leftarrow E \cup \{(\mathbf{x}_{new}, \mathbf{x}_f), \Delta t\}$ 
17    end
18  end
19 end
20  $\mathcal{W} \leftarrow \text{ShortestPath}(G)$ 
21 return  $\mathcal{W}$ 

```

Some discussion regarding the primitives in algorithm 1 is warranted. The primitive *Sample* of line 4 randomly samples the UAV position for a user-specified range of north/east values.

$$\mathbf{x}_{rand} \sim U(\mathbf{x}_{min}, \mathbf{x}_{max}) \quad (119)$$

The primitive *Nearest* finds the vertex in V whose position is closest to \mathbf{x}_{rand} , in an L_2 norm sense.

$$\arg \min_{\mathbf{x}_{nearest}} \|\mathbf{x}_{nearest} - \mathbf{x}_{rand}\| \quad (120)$$

The primitive *Steer* returns a position beginning at $\mathbf{x}_{nearest}$ in the direction of \mathbf{x}_{rand} with a magnitude of λ .

$$\mathbf{x}_{new} = \mathbf{x}_{nearest} + \frac{\mathbf{x}_{rand}}{\|\mathbf{x}_{rand}\|} \lambda \quad (121)$$

The primitive *RunSim* calculates the vehicle trajectory $\mathbf{x}(t)$ by propagating the nonlinear system in Section IV.A from $\mathbf{x}_{nearest}$ to \mathbf{x}_{new} , with all noise terms set to zero. This defines the nominal reference trajectory $\bar{\mathbf{x}}$ to be used in the LinCov simulation. The primitive *ObstacleFree* propagates the augmented system of (27) and (28), as specified by the coefficient matrices of in section IV.B, along the nominal reference trajectory, $\bar{\mathbf{x}}$, producing the covariance of the vehicle state dispersions, D_{true} . The nominal vehicle position trajectory and dispersion covariance are computed as

$$\mathbf{m}_{uav}(t) = A\bar{\mathbf{x}}(t) \quad (122)$$

$$P_{uav} = AD_{true}A^T \quad (123)$$

where

$$A = \left[\begin{array}{cc} I_{2 \times 2} & 0_{2 \times 5} \end{array} \right] \quad (124)$$

and combined with the obstacle means and covariances in \mathcal{O} to yield the system described in Eqs. (108) and (107). The probability of collision is computed at every time-step along the nominal reference trajectory per equation (116). If the probability of collision is below a user-specified threshold, the path is considered free of obstacles. Finally, the primitive *ShortestPath* searches the graph for the shortest distance path from the start vertex \mathbf{x}_s to the final vertex \mathbf{x}_f .

VI. Simulation Results

This section documents the results of the simulation. Section VI.A validates the LinCov model developed in section IV by comparing the trajectory dispersions and estimation errors obtained from Monte Carlo analysis with the covariance computed using the LinCov simulation. Section VI.B demonstrates the augmentation of the RRT path planning algorithm with the uncertain obstacles and UAV position dispersions covariance discussed in section V.

Tables 1 to 4 list the many parameters used in the simulation. The vehicle parameters in Table 1 are based on the Aerosonde UAV [7]. The gust model parameters in Table 2 are based on the Dryden parameters for low altitude and light turbulence [22]. The disturbance torque parameters in Table 2 are not based on physical modeling, but are sized to contribute significantly to the vehicle dispersion and exercise the overall framework. Table 3 defines the noise of the inertial measurement unit and position/velocity sensors. All parameters are typical of GPS-aided inertial navigation systems, with the exception of the gyro noise, which, similar to the disturbance torques, is sized to exercise the developed LinCov and path planning framework. Finally, Table 4 lists the parameters used inside the guidance and control laws.

Table 1 Vehicle Parameters

Parameter	Symbol	Value	Units
Nominal velocity	\bar{V}_g	35.0	m/s
Air density	ρ	1.2682	kg/m^3
Drag coefficient	C_{D_0}	0.03	NA
Planform Area	S_p	0.55	m^2
Mass	m	25.0	kg
Inertial	J	1.759	$kg \cdot m^2$

Table 2 Disturbance Parameters

Parameter	Symbol	Value	Units
Gust stdev	σ_u	1.06	m/s
Gust correlation distance	L_u	200	m
Disturbance torque stdev	σ_T	0.0033	$N \cdot m$
Disturbance torque correlation time	τ_T	2.0	s

Table 3 Sensor Parameters

Parameter	Symbol	Value	Units
Velocity random walk	$\sqrt{S_a}$	0.02	$m/s/\sqrt{hr}$
Angular random walk	$\sqrt{S_\omega}$	16.7	deg/\sqrt{hr}
Position measurement noise	$\sqrt{R_p}$	1.0	m
Velocity measurement noise	$\sqrt{R_v}$	0.033	m/s

Table 4 Controller Parameters

Parameter	Symbol	Value	Units
Velocity proportional gain	P_F	80.0	kg/s
Velocity integral gain	I_F	50.0	kg/s^2
Attitude proportional gain	P_T	6.38	$1/s$
Attitude integral gain	I_T	10.0	$1/s^2$
Attitude derivative gain	D_T	111.0	$kg \cdot m^2/s$
Path control angle	ψ_∞	$\pi/2$	rad
Path control gain	k_{path}	0.05	$1/m$

A. LinCov Validation

This section of the paper serves to validate the Linear Covariance model developed in section VII.A. The method for validation is comparison of the truth state dispersion covariance and the estimation error covariance to the ensemble statistics of a 500 run Monte Carlo simulation. Figure 1 illustrates the scenario used in the validation, which consists of the UAV traveling along a set of waypoints, transitioning in and out of the shaded GPS-denied region, where position and ground speed measurements are unavailable. The black lines show the nominal path of the vehicle, with each individual Monte Carlo run shown in grey.

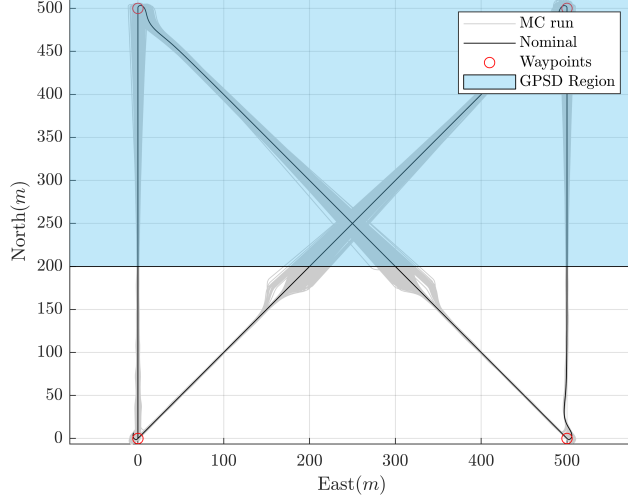


Fig. 1 UAV trajectory with shaded GPS-denied region

Figures 2 and 3 illustrate the position dispersions in the North and East directions. Figures 4 and 5 show similar results but in an Along-Track/Cross-Track coordinate system. The LinCov simulation provides a consistent estimate of vehicle position dispersions, with only occasional outliers occurring upon exiting the GPS-denied region. This is due to the large position dispersions that accrue while inside the GPS-denied region, which cause a variation in the timing of GPS measurement availability. The result is that a small portion of the Monte Carlo runs exit the GPS-denied region late, and therefore receive the first GPS measurement later than the majority of runs. Variable in the timing of events, or "event triggers", is outside the scope of this research, and has been considered in [20]. Figures 6 to 10 show similar results for the remaining truth states.

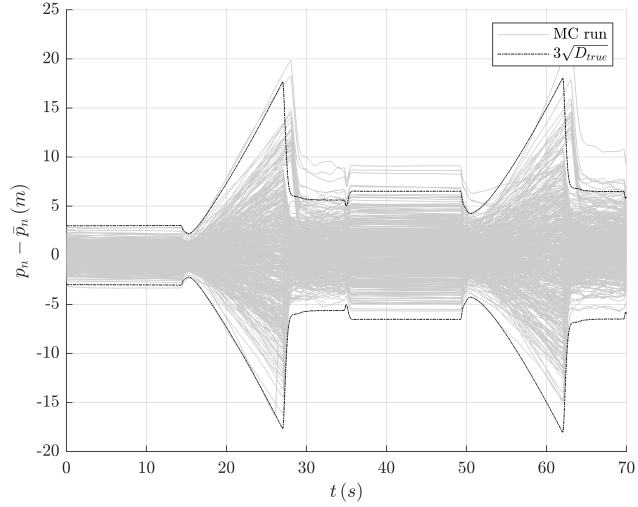


Fig. 2 North position dispersions

Figures 11 to 14 illustrate the estimation errors from the Monte Carlo simulations, the 3σ standard deviation from the EKF, and the 3σ standard deviation derived from the augmented covariance matrix. Excellent agreement is observed

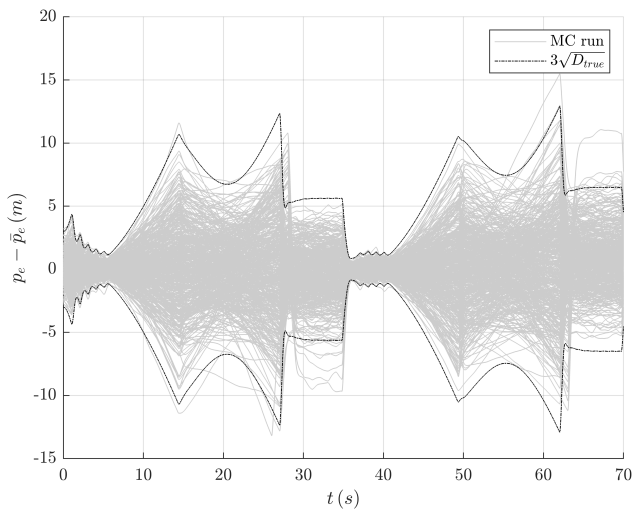


Fig. 3 East position dispersions

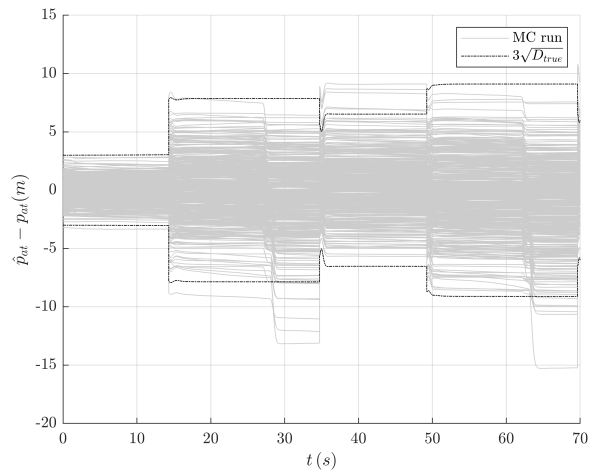


Fig. 4 Along track position dispersions

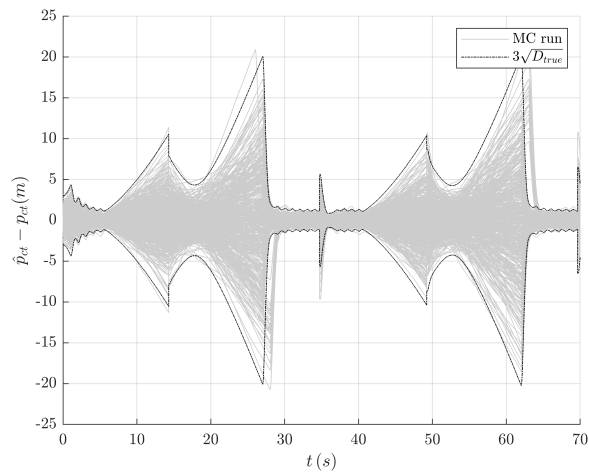


Fig. 5 Cross-track position dispersions

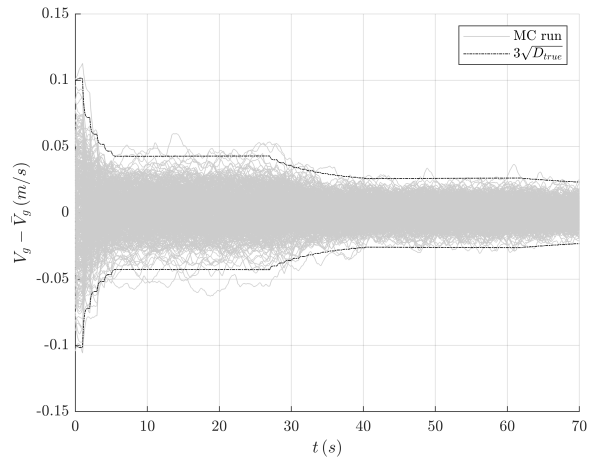


Fig. 6 Ground speed dispersions

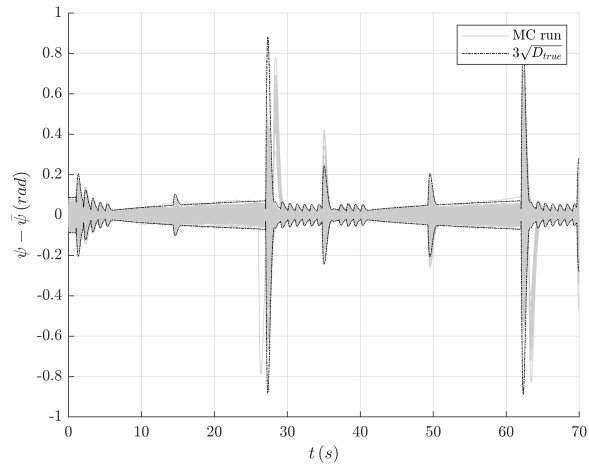


Fig. 7 Heading dispersions

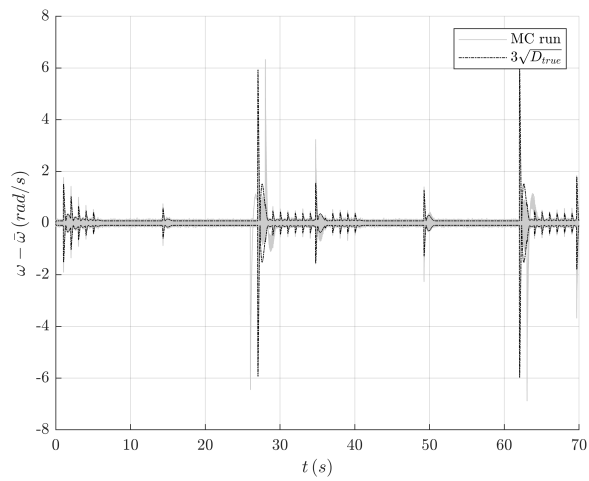


Fig. 8 Angular rate dispersions

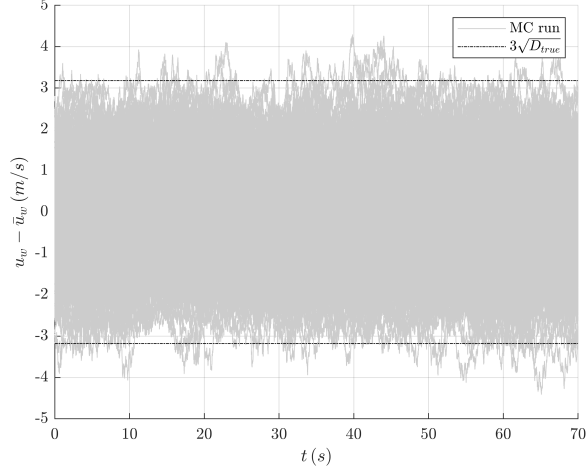


Fig. 9 Wind gust dispersions

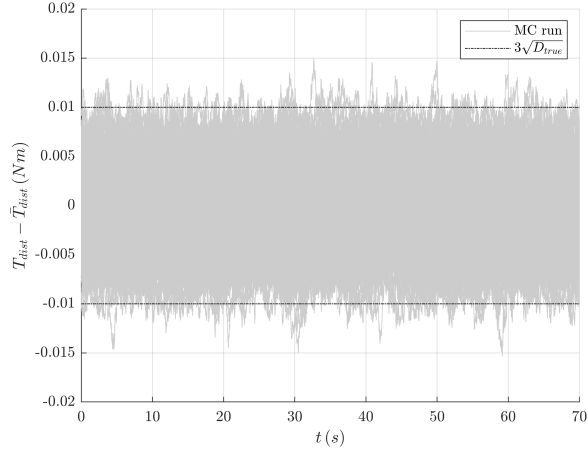


Fig. 10 Disturbance torque dispersions

for all navigation states, suggesting that the EKF is consistent with the truth models in the Monte Carlo simulation and the CL-LinCov framework.

This section illustrates that the developed CL-LinCov framework is consistent with the Monte Carlo simulation. In other words, it produces vehicle dispersion covariances that accurately predict the random variations of the vehicle from the planned path. System analyses, trade studies, sensitivities studies, or, as in the case of this research, path planning can therefore utilize the computed covariances in place of Monte Carlo.

B. Path Planning Demonstration

This section provides an application of the CL-LinCov framework in the RRT path planner for an uncertain obstacle field. Figures 15, 16, and 17 demonstrate the results of a 3000-iteration RRT path planning simulation for three scenarios, where the probability of collision threshold varies from 0.01, 0.001, and 0.0001, respectively. For all scenarios, each obstacle has a location uncertainty of 40 meters 1σ , with a collision distance l set to 10 meters. The UAV begins at

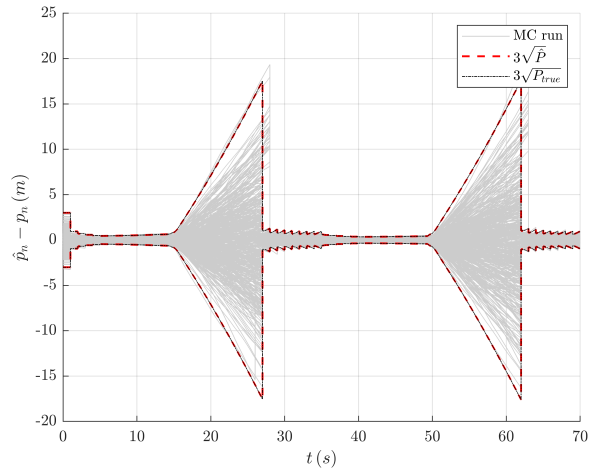


Fig. 11 North position estimation errors

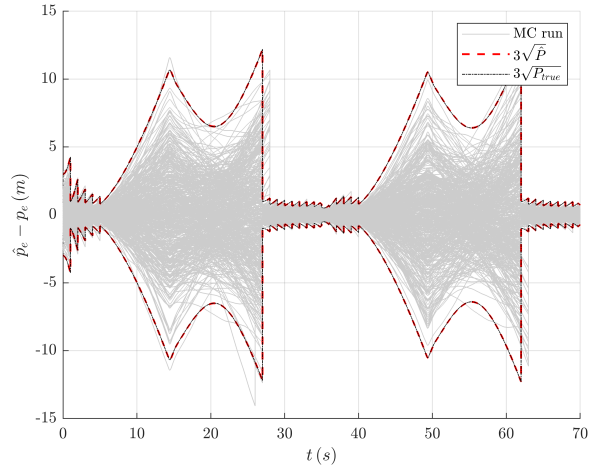


Fig. 12 East position estimation errors

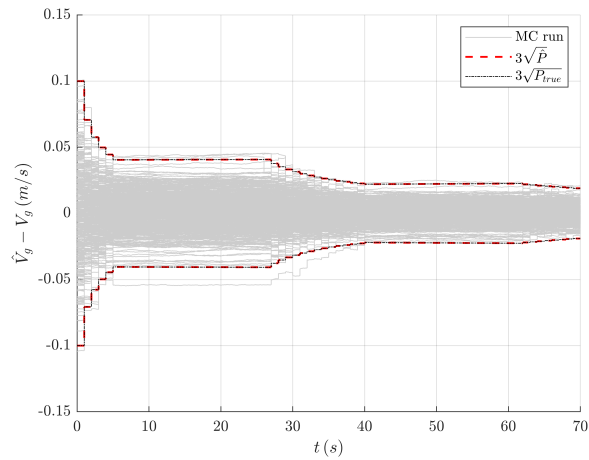


Fig. 13 Ground speed estimation errors

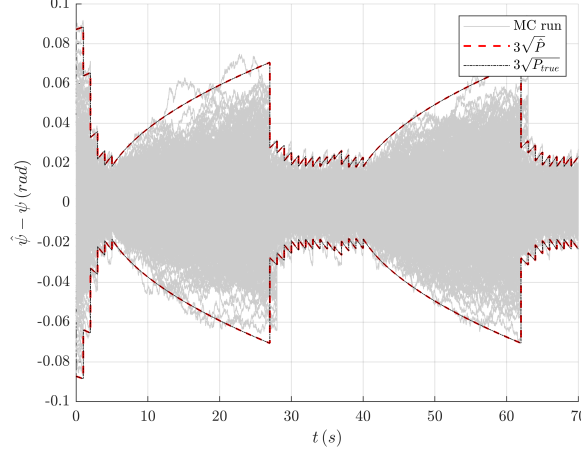


Fig. 14 Heading estimation errors

position [0,0] and is tasked with planning a path to the destination at position [1000,1000]. The blue dots and lines correspond to vertices and edges in the RRT graph. The multi-colored circles correspond to the contours of the Gaussian PDF which defines the location of the obstacle. The red dots and lines correspond to the path in RRT with minimum travel time, i.e. shortest path. The black dashed line represents the nominal reference trajectory, about which the position dispersions are computed. Finally, the shaded region corresponds to an area of GPS-denial, where position and ground speed measurements are not available, causing the vehicle position dispersions to increase over time.

As designed, the RRT algorithm, augmented by knowledge of the UAV position dispersion covariance and obstacle covariance, discovers paths which meet the specified probability of collision threshold. For the large 0.01 threshold value of Figure 15, the path planner considers many possible routes internal to the obstacle field, resulting in a more direct path to the destination. As the probability of collision threshold decreases to 0.001 in Figure 16, the path planner becomes more conservative, only considering paths farther away from the uncertain obstacles. In Figure 17, the path planner has become so conservative, that very few candidate paths exist inside the obstacle field, resulting in the vehicle traveling around the exterior of the obstacles. In all cases, the planned path conforms to the specified probability of collision as verified by Figures 18 to 20.

VII. Conclusion

The ability to quickly plan safe paths in uncertain environments is an enabling technology for wide-spread adoption of autonomous vehicles. This manuscript develops a new closed-loop linear covariance (CL-LinCov) framework which directly computes the dispersion covariance of the vehicle about a candidate path. The framework linearizes the dynamics, guidance, navigation and control equations about the candidate path, accounting for the effects of measurement noise and availability, as well as exogenous disturbances. Two extensions to current CL-LinCov theory were made to accommodate typical GNC algorithm architectures. The first is the separation of the high-level guidance

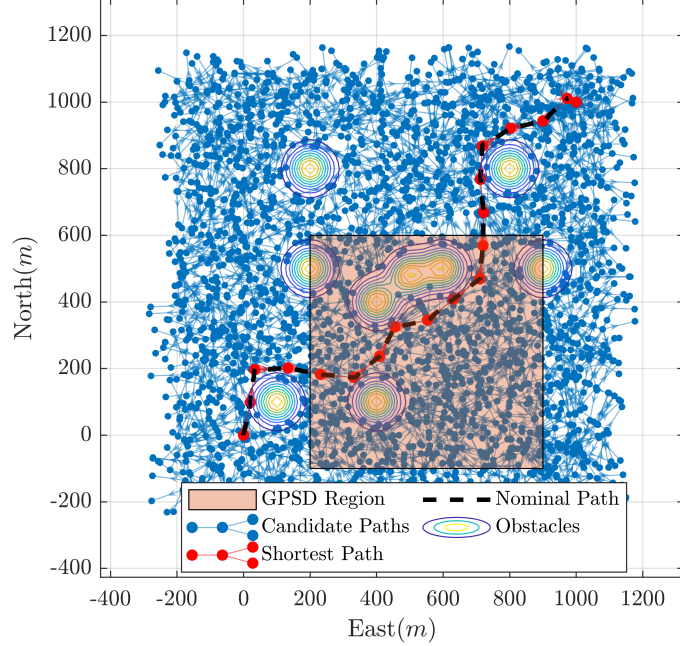


Fig. 15 Path planning Scenario 1: Collision threshold = 0.01

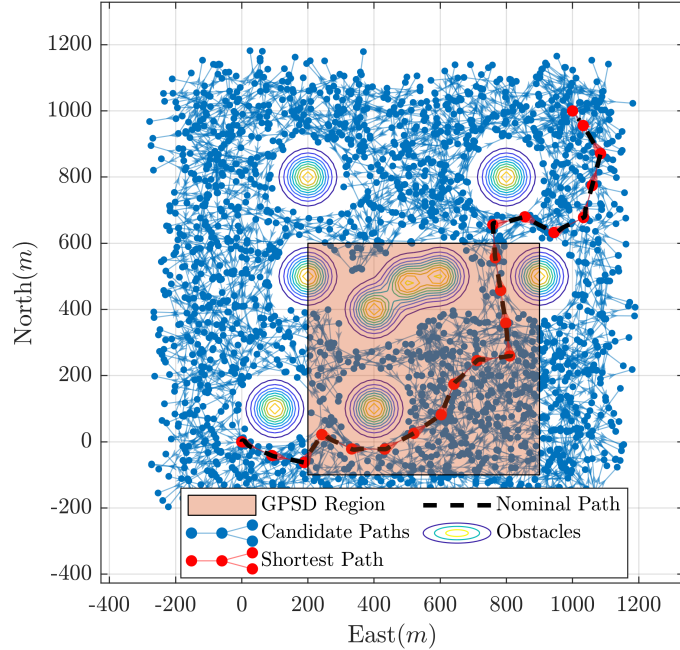


Fig. 16 Path planning Scenario 2: Collision threshold = 0.001

and the low-level control laws. The second is the incorporation of dual-purpose continuous sensors, which are used both in the navigation algorithms for state propagation and in the control law as direct feedback.

The framework is applied to a simplified model of a UAV in the horizontal plane, with straight-line following between way-points, and aided by GPS position and velocity measurements. The consistency of the CL-LinCov results

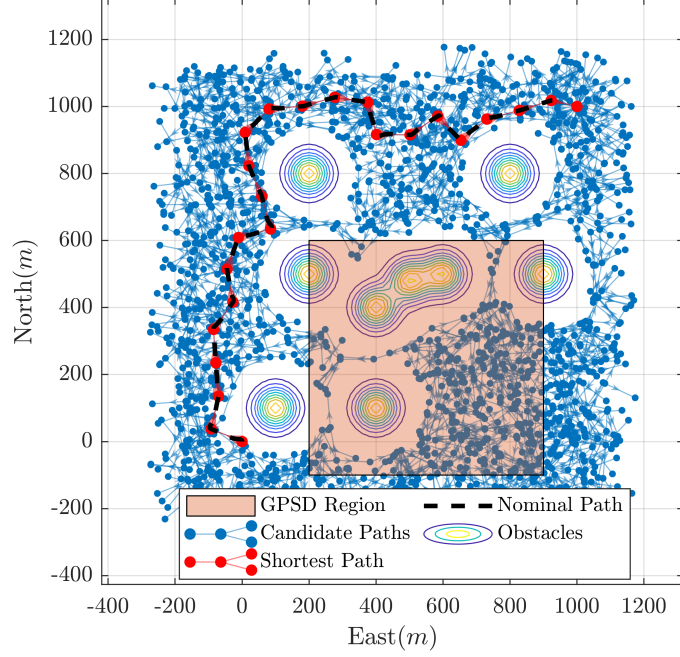


Fig. 17 Path planning Scenario 3: Collision threshold = 0.0001

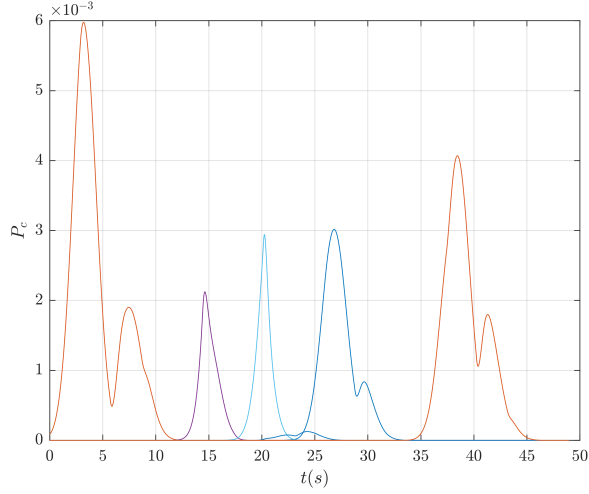


Fig. 18 Collision probabilities for each obstacle, along the lowest-cost path for Scenario 1: Collision threshold = 0.01

is validated via Monte Carlo analysis for a scenario with multiple way-points both inside and outside of a GPS-denied region. As a demonstration of its utility, the CL-LinCov framework is integrated with the rapidly-exploring random tree (RRT) path planning algorithm, in the presence of uncertain obstacles. A linear transformation of the CL-LinCov framework is used to quantify the probability of collision along candidate paths of the RRT. The CL-LinCov + RRT algorithm is shown to identify feasible paths to the destination, while maintaining the probability of collision below user-specified levels.

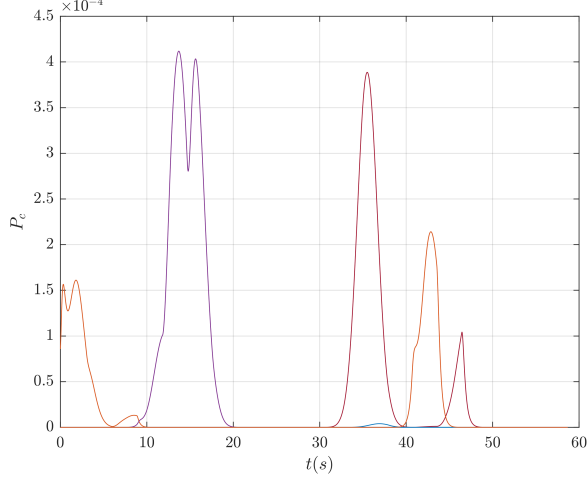


Fig. 19 Collision probabilities for each obstacle, along the lowest-cost path for Scenario 2: Collision threshold = 0.001

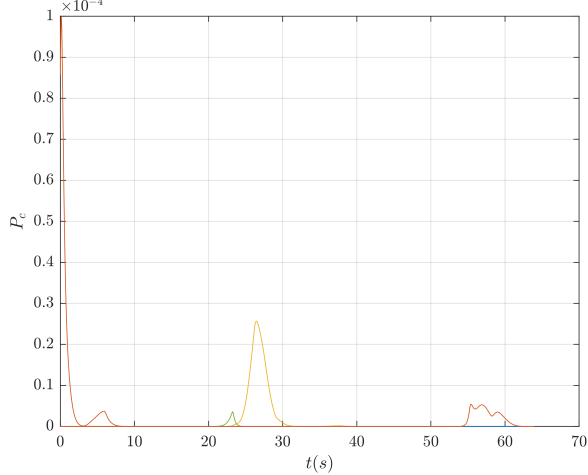


Fig. 20 Collision probabilities for each obstacle, along the lowest-cost path for Scenario 3: Collision threshold = 0.0001

Appendix

A. Linear Covariance Model Derivation

This appendix documents the linearization of the models in section III.A to yield the LinCov framework of section III.B. Linearization of the truth state dynamics Eq. (1), continuous measurements Eq. (2), guidance law Eq. (11), and controller output Eq. (13) yields the following expressions

$$\delta \dot{\mathbf{x}} = F_x \delta \mathbf{x} + F_u \delta \mathbf{u} + B \mathbf{w} \quad (125)$$

$$\delta \tilde{\mathbf{y}} = C_x \delta \mathbf{x} + C_u \delta \mathbf{u} + \boldsymbol{\eta} \quad (126)$$

$$\delta\hat{\mathbf{x}}^* = N_{\hat{x}}\delta\hat{\mathbf{x}} \quad (127)$$

$$\delta\mathbf{u} = G_{\check{x}}\delta\check{\mathbf{x}} + G_{\hat{x}}\delta\hat{\mathbf{x}} + G_{\hat{x}^*}\delta\hat{\mathbf{x}}^* + G_{\check{y}}\delta\check{\mathbf{y}} \quad (128)$$

Substitution of Eq. (126) and Eq. (127) into Eq. (128) yields

$$\delta\mathbf{u} = G_{\check{x}}\delta\check{\mathbf{x}} + (G_{\hat{x}} + G_{\hat{x}^*}N_{\hat{x}})\delta\hat{\mathbf{x}} \quad (129)$$

$$+ G_{\check{y}}C_x\delta\mathbf{x} + G_{\check{y}}C_u\delta\mathbf{u} + G_{\check{y}}\boldsymbol{\eta} \quad (130)$$

Isolation of the control dispersion term yields

$$\delta\mathbf{u} = SG_{\check{x}}\delta\check{\mathbf{x}} + S(G_{\hat{x}} + G_{\hat{x}^*}N_{\hat{x}})\delta\hat{\mathbf{x}} \quad (131)$$

$$+ SG_{\check{y}}C_x\delta\mathbf{x} + SG_{\check{y}}\boldsymbol{\eta} \quad (132)$$

where

$$S = (I_{n_u \times n_u} - G_{\check{y}}C_u)^{-1} \quad (133)$$

Substitution of Eq. (131) into Eq. (125) yields the final form of the linearized truth state dispersion dynamics

$$\delta\dot{\mathbf{x}} = (F_x + F_u SG_{\check{y}}C_x)\delta\mathbf{x} \quad (134)$$

$$+ F_u S(G_{\hat{x}} + G_{\hat{x}^*}N_{\hat{x}})\delta\hat{\mathbf{x}} \quad (135)$$

$$+ F_u SG_{\check{x}}\delta\check{\mathbf{x}} + F_u SG_{\check{y}}\boldsymbol{\eta} + B\mathbf{w} \quad (136)$$

Linearization of the navigation state dynamics Eq. (4) yields

$$\delta\dot{\hat{\mathbf{x}}} = \hat{F}_{\hat{x}}\delta\hat{\mathbf{x}} + \hat{F}_{\check{y}}\delta\check{\mathbf{y}} \quad (137)$$

Substitution of Eq. (127) and Eq. (128) into Eq. (126) yields

$$\delta\check{\mathbf{y}} = C_x\delta\mathbf{x} + C_u G_{\check{x}}\delta\check{\mathbf{x}} \quad (138)$$

$$+ (C_u G_{\hat{x}} + C_u G_{\hat{x}^*}N_{\hat{x}})\delta\hat{\mathbf{x}} \quad (139)$$

$$+ C_u G_{\check{y}}\delta\check{\mathbf{y}} + \boldsymbol{\eta} \quad (140)$$

Isolation of the measurement dispersion term yields

$$\delta\tilde{\mathbf{y}} = TC_x\delta\mathbf{x} + TC_uG_{\hat{x}}\delta\check{\mathbf{x}} \quad (141)$$

$$+ T(C_uG_{\hat{x}} + C_uG_{\hat{x}^*}N_{\hat{x}})\delta\hat{\mathbf{x}} + T\boldsymbol{\eta} \quad (142)$$

where

$$T = \left(I_{n_y \times n_y} - C_uG_{\tilde{\mathbf{y}}} \right)^{-1} \quad (143)$$

Substitution of Eq. (141) into Eq. (137) yields the final form of the linearized navigation state dispersions

$$\delta\dot{\mathbf{x}} = \hat{F}_{\tilde{\mathbf{y}}}TC_x\delta\mathbf{x} \quad (144)$$

$$+ (\hat{F}_{\hat{x}} + \hat{F}_{\tilde{\mathbf{y}}}TC_uG_{\hat{x}} + \hat{F}_{\tilde{\mathbf{y}}}TC_uG_{\hat{x}^*}N_{\hat{x}})\delta\hat{\mathbf{x}} \quad (145)$$

$$+ \hat{F}_{\tilde{\mathbf{y}}}TC_uG_{\hat{x}}\delta\check{\mathbf{x}} + \hat{F}_{\tilde{\mathbf{y}}}T\boldsymbol{\eta} \quad (146)$$

Linearizing the controller state dynamics Eq. (12) yields

$$\delta\dot{\check{\mathbf{x}}} = \check{F}_{\hat{x}}\delta\hat{\mathbf{x}} + \check{F}_{\hat{x}^*}\delta\hat{\mathbf{x}}^* \quad (147)$$

substitution of Eq. (127) into Eq. (147) yields the final form of the controller state dispersion dynamics

$$\delta\dot{\check{\mathbf{x}}} = (\check{F}_{\hat{x}} + \check{F}_{\hat{x}^*}N_{\hat{x}})\delta\hat{\mathbf{x}} \quad (148)$$

The remainder of this derivation linearizes the effect if the Kalman update, which for the controller and truth state dispersions has no effect

$$\delta\mathbf{x}_k^+ = \delta\mathbf{x}_k^- \quad (149)$$

$$\delta\check{\mathbf{x}}_k^+ = \delta\check{\mathbf{x}}_k^- \quad (150)$$

Linearizing the navigation state update Eqs. (3), (5), and Eq. (6) yields

$$\delta\hat{\mathbf{x}}_k^+ = \delta\hat{\mathbf{x}}_k^- + \hat{K}_k [\delta\tilde{\mathbf{z}}_k - \hat{\delta\tilde{\mathbf{z}}}_k] \quad (151)$$

where

$$\delta\tilde{\mathbf{z}}_k = H_x\delta\mathbf{x}_k^- + \boldsymbol{\nu}_k \quad (152)$$

$$\delta\hat{\tilde{\mathbf{z}}}_k = \hat{H}_{\hat{x}}\delta\hat{\mathbf{x}}_k^- \quad (153)$$

Substitution yields the final form of the navigation state dispersion update

$$\delta\hat{\mathbf{x}}_k^+ = (I_{\hat{n} \times \hat{n}} - \hat{K}_k \hat{H}_{\hat{x}}) \delta\hat{\mathbf{x}}_k^- + \hat{K}_k H_x \delta\mathbf{x}_k^- + \hat{K}_k \mathbf{v}_k \quad (154)$$

Funding Sources

This research was funded in part by the U.S. Air Force Research Lab Summer Faculty Fellowship Program

References

- [1] Bry, A., and Roy, N., “Rapidly-exploring Random Belief Trees for motion planning under uncertainty,” *2011 IEEE International Conference on Robotics and Automation*, IEEE, Shanghai, China, 2011, pp. 723–730. <https://doi.org/10.1109/ICRA.2011.5980508>, URL <http://ieeexplore.ieee.org/document/5980508/>.
- [2] Christensen, R. S., and Geller, D., “Linear covariance techniques for closed-loop guidance navigation and control system design and analysis,” *Proceedings of the Institution of Mechanical Engineers, Part G: Journal of Aerospace Engineering*, Vol. 228, No. 1, 2014, pp. 44–65. <https://doi.org/10.1177/0954410012467717>, URL <http://pig.sagepub.com/lookup/doi/10.1177/0954410012467717>.
- [3] LaValle, S. M., and Kuffner, J. J., “Randomized Kinodynamic Planning,” *The International Journal of Robotics Research*, Vol. 20, No. 5, 2001, pp. 378–400. <https://doi.org/10.1177/02783640122067453>, URL <http://journals.sagepub.com/doi/10.1177/02783640122067453>.
- [4] Gammell, J. D., Srinivasa, S. S., and Barfoot, T. D., “Informed RRT*: Optimal sampling-based path planning focused via direct sampling of an admissible ellipsoidal heuristic,” *I*, IEEE, Chicago, IL, 2014, pp. 2997–3004. <https://doi.org/10.1109/IROS.2014.6942976>, URL <https://ieeexplore.ieee.org/document/6942976/>.
- [5] Nasir, J., Islam, F., Malik, U., Ayaz, Y., Hasan, O., Khan, M., and Muhammad, M. S., “RRT*-SMART: A Rapid Convergence Implementation of RRT*,” *International Journal of Advanced Robotic Systems*, Vol. 10, No. 7, 2013, p. 299. <https://doi.org/10.5772/56718>, URL <http://journals.sagepub.com/doi/10.5772/56718>.
- [6] Moon, C.-b., and Chung, W., “Kinodynamic Planner Dual-Tree RRT (DT-RRT) for Two-Wheeled Mobile Robots Using the Rapidly Exploring Random Tree,” *IEEE Transactions on Industrial Electronics*, Vol. 62, No. 2, 2015, pp. 1080–1090. <https://doi.org/10.1109/TIE.2014.2345351>, URL <https://ieeexplore.ieee.org/document/6872545>.
- [7] Beard, Randy, and McLain, Timothy, *Small Unmanned Aircraft Theory and Practice*, 2012.
- [8] Yang, K., Moon, S., Yoo, S., Kang, J., Doh, N. L., Kim, H. B., and Joo, S., “Spline-Based RRT Path Planner for Non-Holonomic Robots,” *Journal of Intelligent & Robotic Systems*, Vol. 73, No. 1-4, 2014, pp. 763–782. <https://doi.org/10.1007/s10846-013-9963-y>, URL <http://link.springer.com/10.1007/s10846-013-9963-y>.

[9] Noreen, I., Khan, A., and Habib, Z., “Optimal Path Planning using RRT* based Approaches: A Survey and Future Directions,” *International Journal of Advanced Computer Science and Applications*, Vol. 7, No. 11, 2016. <https://doi.org/10.14569/IJACSA.2016.071114>, URL <http://thesai.org/Publications/ViewPaper?Volume=7&Issue=11&Code=ijacsa&SerialNo=14>.

[10] Blackmore, L., Ono, M., and Williams, B. C., “Chance-Constrained Optimal Path Planning With Obstacles,” *IEEE Transactions on Robotics*, Vol. 27, No. 6, 2011, pp. 1080–1094. <https://doi.org/10.1109/TRO.2011.2161160>, URL <http://ieeexplore.ieee.org/document/5970128/>.

[11] van den Berg, J., Abbeel, P., and Goldberg, K., “LQG-MP: Optimized path planning for robots with motion uncertainty and imperfect state information,” *The International Journal of Robotics Research*, Vol. 30, No. 7, 2011, pp. 895–913. <https://doi.org/10.1177/0278364911406562>, URL <http://journals.sagepub.com/doi/10.1177/0278364911406562>.

[12] Jin, K., Geller, D. K., and Luo, J., “Robust Trajectory Design for Rendezvous and Proximity Operations with Uncertainties,” *Journal of Guidance, Control, and Dynamics*, Vol. 43, No. 4, 2020, pp. 741–753. <https://doi.org/10.2514/1.G004121>, URL <https://arc.aiaa.org/doi/10.2514/1.G004121>.

[13] Zhu, H., and Alonso-Mora, J., “Chance-Constrained Collision Avoidance for MAVs in Dynamic Environments,” *IEEE Robotics and Automation Letters*, Vol. 4, No. 2, 2019, pp. 776–783. <https://doi.org/10.1109/LRA.2019.2893494>, URL <http://ieeexplore.ieee.org/document/8613928/>.

[14] Shetty, A., and Gao, G. X., “Trajectory Planning Under Stochastic and Bounded Sensing Uncertainties Using Reachability Analysis,” 2020, pp. 1637–1648. <https://doi.org/10.33012/2020.17518>, URL <https://www.ion.org/publications/abstract.cfm?articleID=17518>.

[15] Christensen, R. S., and Geller, D. K., “Closed-Loop Linear Covariance Analysis for Hosted Payloads,” *Journal of Guidance, Control, and Dynamics*, Vol. 41, No. 10, 2018, pp. 2133–2143. <https://doi.org/10.2514/1.G003333>, URL <https://arc.aiaa.org/doi/10.2514/1.G003333>.

[16] Geller, D. K., “Linear Covariance Techniques for Orbital Rendezvous Analysis and Autonomous Onboard Mission Planning,” *Journal of Guidance, Control, and Dynamics*, Vol. 29, No. 6, 2006, pp. 1404–1414. <https://doi.org/10.2514/1.19447>, URL <http://arc.aiaa.org/doi/10.2514/1.19447>.

[17] Woffinden, D., Robinson, S., Williams, J., and Putnam, Z. R., “Linear Covariance Analysis Techniques to Generate Navigation and Sensor Requirements for the Safe and Precise Landing Integrated Capabilities Evolution (SPLICE) Project,” *AIAA Scitech 2019 Forum*, American Institute of Aeronautics and Astronautics, San Diego, California, 2019. <https://doi.org/10.2514/6.2019-0662>, URL <https://arc.aiaa.org/doi/10.2514/6.2019-0662>.

[18] Christensen, D., and Geller, D., “Terrain-Relative and Beacon-Relative Navigation for Lunar Powered Descent and Landing,” *The Journal of the Astronautical Sciences*, Vol. 58, No. 1, 2011, pp. 121–151. <https://doi.org/10.1007/BF03321162>, URL <http://link.springer.com/10.1007/BF03321162>.

[19] Christensen, R., Geller, D., and Hansen, M., “Linear Covariance Navigation Analysis of Range and Image Measurement Processing for Autonomous Lunar Lander Missions,” *2020 IEEE/ION Position, Location and Navigation Symposium (PLANS)*, IEEE, Portland, OR, USA, 2020, pp. 1524–1535. <https://doi.org/10.1109/PLANS46316.2020.9109838>, URL <https://ieeexplore.ieee.org/document/9109838/>.

[20] Geller, D. K., Rose, M. B., and Woffinden, D. C., “Event Triggers in Linear Covariance Analysis with Applications to Orbital Rendezvous,” *Journal of Guidance, Control, and Dynamics*, Vol. 32, No. 1, 2009, pp. 102–111. <https://doi.org/10.2514/1.36834>, URL <http://arc.aiaa.org/doi/10.2514/1.36834>.

[21] Maybeck, P. S., *Stochastic Models, Estimation, and Control*, Vol. 1, Navtech Book and Software Store, New York, 1994.

[22] Langelaan, J. W., Alley, N., and Neidhoefer, J., “Wind Field Estimation for Small Unmanned Aerial Vehicles,” *Journal of Guidance, Control, and Dynamics*, Vol. 34, No. 4, 2011, pp. 1016–1030. <https://doi.org/10.2514/1.52532>, URL <https://arc.aiaa.org/doi/10.2514/1.52532>.

[23] Park, J. S., Park, C., and Manocha, D., “Efficient probabilistic collision detection for non-convex shapes,” *2017 IEEE International Conference on Robotics and Automation (ICRA)*, IEEE, Singapore, Singapore, 2017, pp. 1944–1951. <https://doi.org/10.1109/ICRA.2017.7989226>, URL <http://ieeexplore.ieee.org/document/7989226/>.

[24] Park, C., Park, J. S., and Manocha, D., “Fast and Bounded Probabilistic Collision Detection in Dynamic Environments for High-DOF Trajectory Planning,” *arXiv:1607.04788 [cs]*, 2016. URL <http://arxiv.org/abs/1607.04788>, arXiv: 1607.04788.

[25] Sun, W., Torres, L. G., van den Berg, J., and Alterovitz, R., “Safe Motion Planning for Imprecise Robotic Manipulators by Minimizing Probability of Collision,” *Robotics Research*, Vol. 114, edited by M. Inaba and P. Corke, Springer International Publishing, Cham, 2016, pp. 685–701. https://doi.org/10.1007/978-3-319-28872-7_39, URL http://link.springer.com/10.1007/978-3-319-28872-7_39, series Title: Springer Tracts in Advanced Robotics.

[26] Axelrod, B., Kaelbling, L. P., and Lozano-Pérez, T., “Provably safe robot navigation with obstacle uncertainty,” *The International Journal of Robotics Research*, Vol. 37, No. 13-14, 2018, pp. 1760–1774. <https://doi.org/10.1177/0278364918778338>, URL <http://journals.sagepub.com/doi/10.1177/0278364918778338>.

[27] Wu, P., Li, L., Xie, J., and Chen, J., “Probabilistically Guaranteed Path Planning for Safe Urban Air Mobility Using Chance Constrained RRT*,” *AIAA AVIATION 2020 FORUM*, American Institute of Aeronautics and Astronautics, VIRTUAL EVENT, 2020. <https://doi.org/10.2514/6.2020-2914>, URL <https://arc.aiaa.org/doi/10.2514/6.2020-2914>.

[28] Karaman, S., and Frazzoli, E., “Incremental Sampling-based Algorithms for Optimal Motion Planning,” *arXiv:1005.0416 [cs]*, 2010. URL <http://arxiv.org/abs/1005.0416>, arXiv: 1005.0416.